Journal of Power Sources 208 (2012) 345–353

Contents lists available at SciVerse ScienceDirect

Journal of Power Sources

journal homepage: www.elsevier.com/locate/jpowsour

# Highly conductive electrospun carbon nanofiber/$MnO_2$ coaxial nano-cables for high energy and power density supercapacitors

Mingjia Zhi[a], Ayyakkannu Manivannan[b], Fanke Meng[a], Nianqiang Wu[a,*]

[a] Department of Mechanical & Aerospace Engineering, WVNano Initiative, West Virginia University, Morgantown, WV 26506-6106, USA
[b] National Energy Technology Laboratory, U.S. Department of Energy, 3610 Collins Ferry Road, Morgantown, WV 26507, USA

ARTICLE INFO

*Article history:*
Received 3 December 2011
Received in revised form 14 February 2012
Accepted 15 February 2012
Available online 23 February 2012

*Keywords:*
Supercapacitor
Electrospinning
$MnO_2$
Impedance
Carbon nanofibers

ABSTRACT

This paper presents highly conductive carbon nanofiber/$MnO_2$ coaxial cables in which individual electrospun carbon nanofibers are coated with an ultrathin hierarchical $MnO_2$ layer. In the hierarchical $MnO_2$ structure, an around 4 nm thick sheath surrounds the carbon nanofiber (CNF) in a diameter of 200 nm, and nano-whiskers grow radically outward from the sheath in view of the cross-section of the coaxial cables, giving a high specific surface area of $MnO_2$. The CNFs are synthesized by electrospinning a precursor containing iron acetylacetonate (AAI). The addition of AAI not only enlarges the specific surface area of the CNF but also greatly enhances their electronic conductivity, which leads to a dramatic improvement in the specific capacitance and the rate capability of the CNF/$MnO_2$ electrode. The AAI-CNF/$MnO_2$ electrode shows a specific capacitance of 311 F $g^{-1}$ for the whole electrode and 900 F $g^{-1}$ for the $MnO_2$ shell at a scan rate of 2 mV $s^{-1}$. Good cycling stability, high energy density (80.2 Wh $kg^{-1}$) and high power density (57.7 kW $kg^{-1}$) are achieved. This work indicates that high electronic conductivity of the electrode material is crucial to achieving high power and energy density for pseudo-supercapacitors.

© 2012 Elsevier B.V. All rights reserved.

## 1. Introduction

Among various types of electrochemical energy storage devices, supercapacitors have desirable characteristics such as rapid charging time, high cycling stability and good temperature stability. Supercapacitors have a potential to achieve a wide range of energy and power densities, that is, have the largest area on a Ragone plot. For traditional carbon-based electrochemical double-layer capacitors (EDLC), the maximum capacitance is restricted by the active electrode surface area and the pore size distribution (typically 40 μF $cm^{-2}$, or ~150 F $g^{-1}$ for carbon) [1–4]. To increase the energy density, transitional metal oxides such as NiO, $RuO_2$ and $MnO_2$ have been introduced for the pseudocapacitance due to their fast surface redox properties [5–10]. Among the metal oxides investigated so far, $MnO_2$ is one of the best candidates because of its high theoretical specific capacitance (~1370 F $g^{-1}$), low environmental toxicity and low cost. Unfortunately the poor electrical conductivity of $MnO_2$ limits the full utilization of its high pseudocapacitance [11,12].

In order to increase the electrical conductivity of the $MnO_2$ based electrodes, $MnO_2$ are dispersed on the conductive backbone so that the electrical current can flow through the backbone to $MnO_2$ to accomplish the charge storage reaction. The key to success is forming a high surface-area metal oxide layer while preserving high conductivity of the electrode even at a high oxide loading. Various supporting backbones have been reported for $MnO_2$, including carbon nanotubes (CNT) [13–15], graphene [16,17], polyaniline (PANi) [18], carbon nanofoam [19], carbon nanocoil [20], porous metal [21] and conductive oxide [22–24]. Specific capacitances of 400–1200 F $g^{-1}$ have been achieved for pristine $MnO_2$ in the above investigations. Recently, electrospun carbon nanofibers (CNF) have been considered as the promising conductive support for metal oxides due to their high surface area, excellent mechanical property and low cost of synthesis [25,26]. For example, an ultrathin $V_2O_5$ film was electrodeposited on the free-standing activated CNF paper and exhibited 1307 F $g^{-1}$ specific capacitance for $V_2O_5$, which is the highest shown in literature as of today [25]. The carbon/$MnO_2$ coaxial nanocomposite also showed 539 F $g^{-1}$ of specific capacitance at 0.38 mg $cm^{-2}$ of $MnO_2$ loading [26]. However, such high capacitance values can be obtained only at a very slow scan rate (2 mV $s^{-1}$) and or at a low metal oxide loading (<10 wt%). Large performance loss occurs at a high scan rate or at a high metal oxide loading, which hinders their practical application when both high power and energy densities are required. Moreover, no detailed studies have been performed to reveal the origin of such degradation behavior or to offer a solution to the drawbacks.

In the present work, individual electrospun carbon nanofibers are coated with an ultrathin hierarchical $MnO_2$ layer to form coaxial nano-cables. In the hierarchical $MnO_2$ structure, an around 4 nm thick sheath surrounds the CNF, and billions of nano-whiskers grow

* Corresponding author. Tel.: +1 304 293 3326; fax: +1 304 293 6689.
*E-mail address:* nick.wu@mail.wvu.edu (N. Wu).

0378-7753/$ – see front matter © 2012 Elsevier B.V. All rights reserved.
doi:10.1016/j.jpowsour.2012.02.048

radically outward from the sheath in view of the cross-section of the coaxial cables, which gives a high specific surface area of $MnO_2$. In order to improve the electrical conductivity of the CNFs, a small amount of iron acetylacetonate (AAI) is incorporated into the electrospun precursor, which not only enlarges the specific surface area of the CNFs but also greatly enhances their electronic conductivity. As a result, the specific capacitance and the rate capability electrode are improved dramatically. Here we have demonstrated a simple, inexpensive and scale-up method that is performed at an ambient condition for fabrication of a $MnO_2$–based electrode for a high power and energy density pseudo-supercapacitor. A comparative investigation is conducted on the AAI-incorporated CNF and the conventional CNF $MnO_2$/CNF electrode. In addition, electrochemical impedance spectroscopy (EIS) is introduced to study the correlation of the pseudocapacitance performance with the electronic conductivity of the CNF backbone.

## 2. Experimental

### 2.1. Electrode preparation

Carbon nanofibers were prepared by electrospinning method and following carbonization process [27]. 10 wt% of polyacrylonitrile (PAN) was first dissolved in N,N-Dimethylformamide (DMF) at 80 °C under stirring. Iron acetylacetonate (AAI) was then added (2% to the total solution mass) to form the precursor. The electrospinning was conducted in a homemade apparatus, the precursor feeding rate was 1 ml $h^{-1}$ and the electrical field was 1.2 kV $cm^{-1}$. The distance between the needle and the metal collector was fixed at 15 cm. The as spun fiber mats were heated to 280 °C in air in 5 °C $min^{-1}$ heating rate and kept for 1 h. Afterward the nanofibers were carbonized at 850 °C in $N_2$ flow. The carbonized nanofibers were then immersed in 1 M HCl solution for 1 h to remove the residue surface iron compound content and washed with $H_2O$ and ethanol for several times. Such carbon nanofibers are denoted as AAI-CNF.

$MnO_2$ coating was conducted by immersing the AAI-CNF sheets into $KMnO_4$ solution at 60 °C. The weight ratio of AAI-CNF to $KMnO_4$ varied from 4:1, 2:1 1:1 and 1:2. AAI-CNF core/$MnO_2$ shell structure was formed in this process thus the samples are denoted as AAI-CNF@$MnO_2$ 1, 2, 3, and 4. The immersing process was finished until the purple color of the $MnO_4^-$ disappeared. The residue solution color was golden brown. The resulted $MnO_2$ coated AAI-CNF sheets were then rinsed in $H_2O$ for several times to remove the byproduct. A series of samples using regular CNF without AAI loading were prepared in identical way for comparison and denoted as CNF@$MnO_2$.

### 2.2. Materials characterizations

The morphology of the electrodes was observed using a JEOL 7600F scanning electron microscope (SEM) and a JEOL JEM 2100F transmission electron microscope (TEM). The chemical structure of $MnO_2$ was characterized using a PHI 5000 Versa Probe X-ray photoelectron spectroscopy (XPS). The specific surface area of the CNFs was measured using TriStar II 3020 absorption/desorption analyzer with $N_2$ at 77 K. Raman spectra of the carbon nanofibers were obtained with Renishaw Raman Spectroscopy. Thermal gravimetric analysis (TGA) was used to determine the $MnO_2$ mass content in the electrodes. The sample was heated to 800 °C in air at a rate of 10 °C $min^{-1}$ and isothermally held for 2 h. The crystalline structures of the samples were characterized using PANalytical X-ray diffraction (XRD) instrument with a Cu kα radiation. The surface functional group of the carbon nanofibers were measured using Fourier transform infrared spectroscopy (FTIR) with a NEXUS 870 spectrometer. The electronic conductivity was measured using 2 probes method, and the conductivity $\sigma$ was calculated by $\sigma = L/A^*R$, in which $L$ and $A$ are the length and the cross section area of the electrode and $R$ is the measured resistance.

### 2.3. Electrochemical testing

The electrochemical testing was performed using three electrodes configuration using Gamry Reference 600 Potentiostat. The AAI-CNF@$MnO_2$ and CNF@$MnO_2$ sheets were directly used as the working electrodes in 1 M $Na_2SO_4$ electrolyte. Pt wire and Ag/AgCl electrode were used as the counter and reference electrodes, respectively. The electrochemical characterization was performed using cyclic voltammetry (CV), galvanostatic charge–discharge and electrochemistry impedance (EIS) method. The voltage window was −0.2 V to 0.8 V versus Ag/AgCl. The EIS was collected at open circuit condition from 10 mHz to 1 MHz with AC amplitude of 10 mV. The specific capacitance in CV was calculated as $C = \int Idt/V$, where $I$ is the current, $V$ is the working potential window and m is the mass of the electrode. The integrating process was performed by Echem Analyst software.

The specific capacitance derived from galvanostatic testing was calculated by $C = It/Vm$, where $I$ is the discharge current, $t$ is the discharge time, $V$ is the working potential window and $m$ is the mass of the electrode. The energy density ($E$) and the power density ($P$) were derived from galvanostatic testing using equations

$E = CV^2/2$ and $P = E/t$, where $C$ is the specific capacitance, $V$ is the working potential window and $t$ is the discharge time.

## 3. Results and discussion

Fig. 1(a) shows the SEM image of the as-carbonized PAN nanofibers with the AAI additive. The nanofibers were around 200 nm in a diameter and were uniform. Some small nanoparticles were decorated on the surface of the nanofibers, which were believed to be the iron oxide phase ($Fe_3O_4$) derived from the decomposition of AAI in the carbonization process [27]. After the nanofibers were washed with HCl, the CNF surface became clean as shown in Fig. 1(b), since the particles were etched away. The surface area of the acid-washed AAI-CNF (102 $m^2$ $g^{-1}$) was larger than that of the regular CNF (28 $m^2$ $g^{-1}$) because the nanofibers surface became more rough. This observation was consistent with the result reported previously [27]. After the AAI-CNF sheets were incubated in the $KMnO_4$ solution, $MnO_2$ was deposited on the CNF surface due to the well known reaction [15]

$$3C + 4MnO_4^- + H_2O = 4MnO_2 + 2HCO_3^- + CO_3^{2-} \quad (1)$$

During reaction, the outer layer carbon was gradually substituted by $MnO_2$. The porosity of the fiber network was retained. Fig. 1(c) shows the SEM image of the AAI-CNF@$MnO_2$ 1. It is clearly evident that the squama-like $MnO_2$ textures appeared on the CNF surface. When the amount of $KMnO_4$ increased as that the AAI-CNF:$KMnO_4$ weight ratio was 1:2, the $MnO_2$ shell covered the whole CNF surface and became more homogeneous (Fig. 1(d)). The CNF diameter also increased with an increase in the $MnO_2$ coverage. It should be noted that the experiments were carried out in a neutral condition, which prevented from the $MnO_2$ agglomeration [19]. The TEM image in Fig. 1(e) shows the core-shell structure of the AAI-CNF@$MnO_2$ (Sample 3). The ~20 nm sized particles were the residual iron compound. A porous $MnO_2$ shell was coated on the CNF surface. A closer view in Fig. 1(f) reveals that ~40 nm long nano-whiskers grow radically outward.

The crystal structure of the coated $MnO_2$ was examined with XRD. Fig. 2(a) shows the diffraction patterns of AAI-CNF@$MnO_2$ (sample 3). Besides graphite, magnetite ($Fe_3O_4$) and birnessite type $MnO_2$ were found, which confirmed that the $MnO_2$ shell

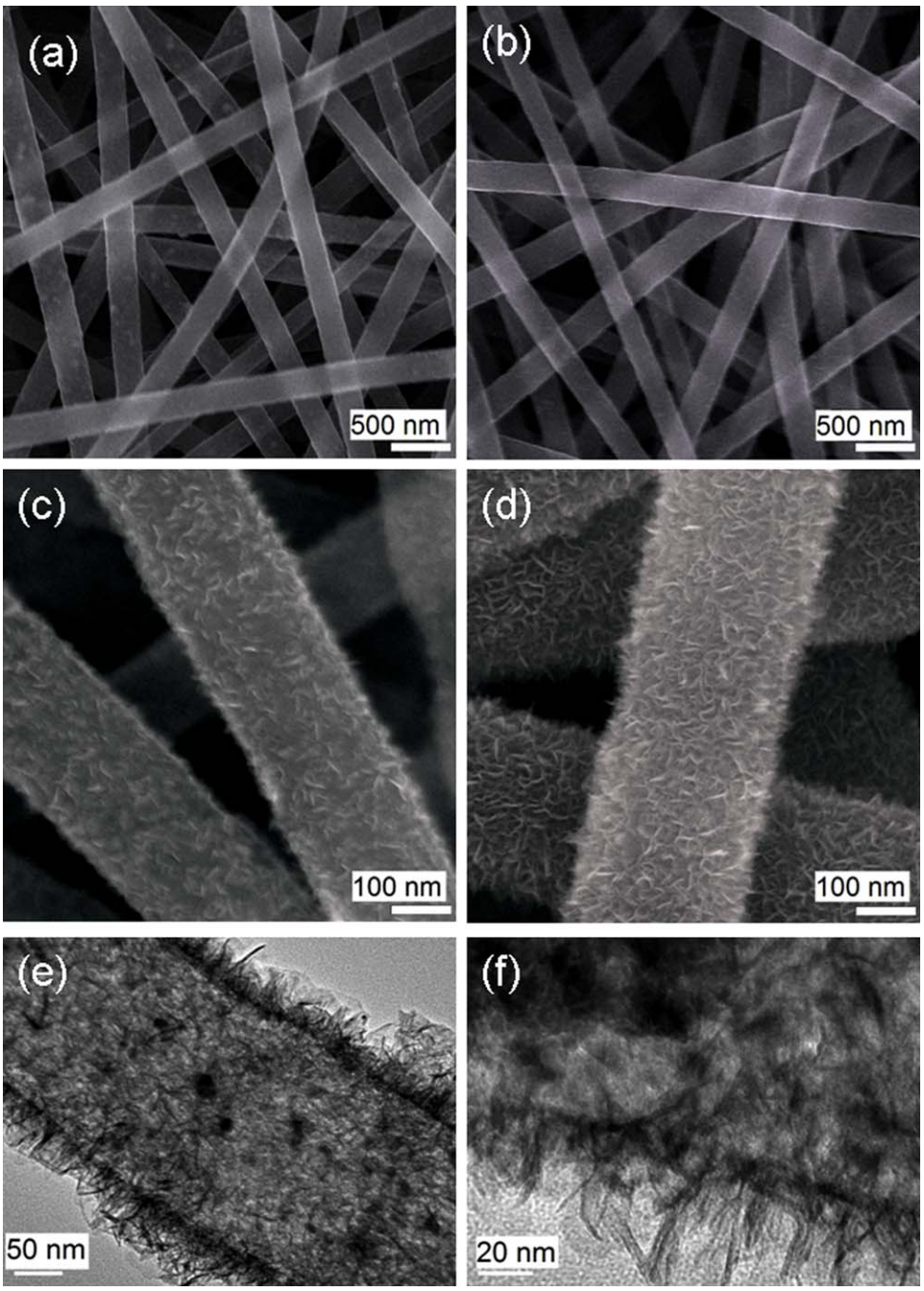


**Fig. 1.** SEM images of the AAI-CNF and the AAI-CNF@$MnO_2$ composite. (a) AAI-CNF before acid washing, (b) AAI-CNF after acid washing, (c) AAI-CNF@$MnO_2$ electrode 1 and (d) AAI-CNF@$MnO_2$ electrode 4; (e) TEM images of a single AAI-CNF@$MnO_2$ nanostructure and (f) the $MnO_2$ porous shell with nanowhiskers.

was crystallized although the broad diffraction peaks indicated poor crystallinity. Similar results have been reported in the graphene/$MnO_2$ mixture previously [28]. After heat treatment in air at 800 °C for 3 h, the residue of the sample was confirmed to be a mixture of $Mn_2O_3$ and $Fe_2O_3$, as shown in Fig. 2(a). The mass loading of $MnO_2$ was calculated by TGA method. Table 1 shows that the $MnO_2$ mass loading in four samples were about 13.9%, 23.0%, 39.1% and 59.0%, respectively. These numbers were close to the theoret-

**Table 1**
TGA results of the AAI-CNF@$MnO_2$ samples and the calculation of $MnO_2$ mass ratio.[a]

| Sample | As carbonized AAI-CNF | HCl washed AAI-CNF | AAI-CNF@$MnO_2$ 1 | AAI-CNF@$MnO_2$ 2 | AAI-CNF@$MnO_2$ 3 | AAI-CNF@$MnO_2$ 4 |
|---|---|---|---|---|---|---|
| Residue mass | 0.137 | 0.083 | 0.211 | 0.290 | 0.438 | 0.619 |
| $MnO_2$ content | 0 | 0 | 0.139 | 0.230 | 0.391 | 0.590 |
| Theoretical $MnO_2$ content | 0 | 0 | 0.124 | 0.224 | 0.379 | 0.580 |

[a] The $MnO_2$ content is calculated as following:
$MnO_2$ content = (residue mass in $MnO_2$ coated sample − residue mass in acid washed AAI-CNF)/79*87, the residue $MnO_2$ is transferred to $Mn_2O_3$ at 800 °C.
The $MnO_2$ content in CNF@$MnO_2$ samples are assumed to be the theoretical number.

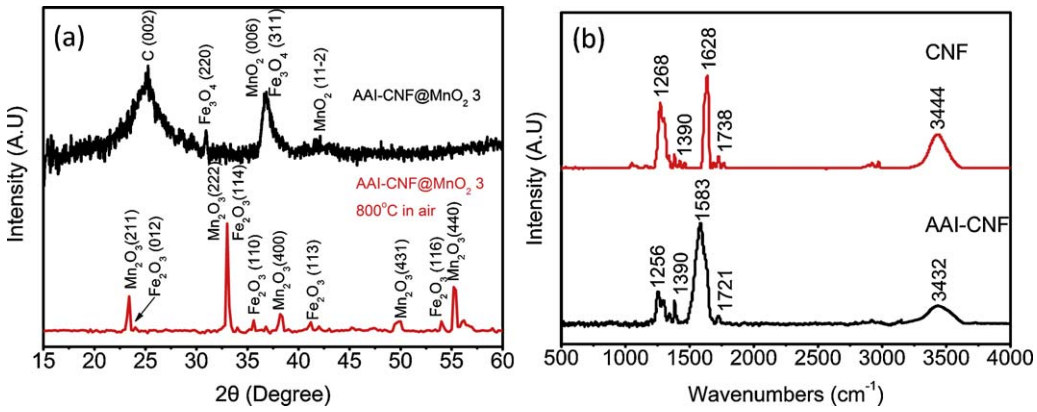


**Fig. 2.** (a) XRD spectra of the as-prepared AAI-CNF@$MnO_2$ (sample 3) and after heat treatment in air at 800 °C, (b) FTIR spectra of the AAI-CNF and the CNF.

ical ratio calculated from Reaction (1), which indicated a complete conversion of $KMnO_4$ to $MnO_2$.

The surface functional groups of the AAI-CNF and the CNF were also examined with FTIR spectroscopy (Fig. 2(b)). The broad peaks at ~3400 $cm^{-1}$ was assigned to the O—H stretch due to the surface adsorbed moisture. The C=O stretch band were indicated at around 1730 $cm^{-1}$ [29]. It is worth noting that the relative intensity of the asymmetric $\nu_{as}$ $COO^-$ (~1560 $cm^{-1}$) and symmetric $\nu_s$ $COO^-$ (~1400 $cm^{-1}$) bands for the AAI-CNF was higher than CNF, due to the carboxylate groups brought by acid treatment. The band at ~1260 $cm^{-1}$ could be attributed to the C—O stretch [29].

XPS was used to examine the chemical valence state of Mn. Fig. 3(a) reveals the Mn 3s core-level spectra of four AAI-CNF@$MnO_2$ samples. It is known that the oxidation state of Mn can be determined from the separation of the 3s peaks [23,26]. For all the samples, the separation of the Mn 3s peaks was 4.95 eV, which suggested the average oxidation state of the manganese oxide was 3.6 [23,26]. A weak peak at 532 eV in the O 1s core-level was observed before $MnO_2$ coating (Fig. 3(b)), which was assigned to the surface-adsorbed $H_2O$ and other oxygen specie. A strong peak at 530 eV was ascribed to the lattice oxygen in $MnO_2$ in the samples immersed in $KMnO_4$ solution.

Cyclic voltammetry (CV) was used to measure the electrochemical charge storage capacity of the electrode. Fig. 4(a) shows the CV curves of the AAI-CNF/$MnO_2$ electrodes taken at a scan rate of 100 mV $s^{-1}$. The AAI-CNF@$MnO_2$ electrodes 1 and 2 showed nearly symmetrical box-like shape, indicating a good capacitor characteristic. The AAI-CNF@$MnO_2$ electrode 3 had the highest specific current density with a moderate disordered rectangular shape. When the $MnO_2$ mass loading increased to 59% in AAI-CNF@$MnO_2$ (Sample 4), the gravimetric current density decreased and the CV shape was further disordered. Overall an ideal capacitive character can be well maintained up to the scan rate of 200 mV $s^{-1}$ for AAI-CNF@$MnO_2$ 1 and 2 whereas moderate disordered CV curves were observed for AAI-CNF@$MnO_2$ 3 and 4. In contrast, the CNF@$MnO_2$ electrodes in the absence of AAI exhibited very different trends as shown in Fig. 4(b). Only CNF@$MnO_2$ 1 displayed an acceptable CV shape but the other electrodes with higher $MnO_2$ loading severely deviated from the ideal capacitor behavior, as the CV curves became "diamond" shape. The current density was also much lower than that of the AAI-CNF@$MnO_2$ series.

Fig. 4(c) and (d) shows the comparison of the specific capacitance of the electrodes with and without AAI. The AAI-CNF itself had ~32 F $g^{-1}$ capacitance at 2 mV $s^{-1}$ scan, which was 5 times higher than the CNF. An excellent rate capability of 90% was retained up to 200 mV $s^{-1}$ scan. This value was comparable to most activated carbon nanofiber electrodes although the capacitance was lower due to the lack of the pore size engineering. The specific capacitance jumped to 140 F $g^{-1}$ for the AAI-CNF@$MnO_2$ electrode (Sample 1) at 2 mV $s^{-1}$ scan and dropped to 106 F $g^{-1}$ at 200 mV $s^{-1}$ scan, which retained 76% of the capacity. When the $MnO_2$ loading increased up to 39% (Sample 3), the AAI-CNF@$MnO_2$ electrode possessed 311 F $g^{-1}$ of capacitance at 2 mV $s^{-1}$, and the capacity retention of 51% was achieved at 200 mV $s^{-1}$. These values were greater than the CNF@$V_2O_5$ coaxial nanofibers (214 F $g^{-1}$ at 2 mV $s^{-1}$, ~58% retain at 50 mV $s^{-1}$) [25], $MnO_2$/graphene (~43% retain) [16,17] and the layer-by-layer CNT-$MnO_2$ assembly (290 F $g^{-1}$) [13]. The specific capacitance dropped to 216 F $g^{-1}$ and the rate capability reduced to 26% when the $MnO_2$ loading increased to 59%. In contrast, the CNF@$MnO_2$ electrodes showed much poorer perfor-

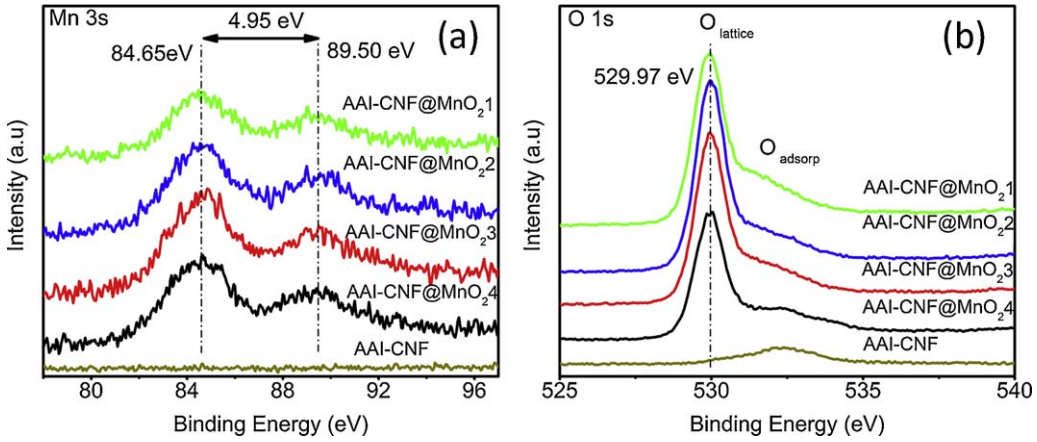


**Fig. 3.** XPS spectra of the AAI-CNF/$MnO_2$ coaxial cable electrodes, (a) the Mn 3s core-level and (b) the O 1s core-level.

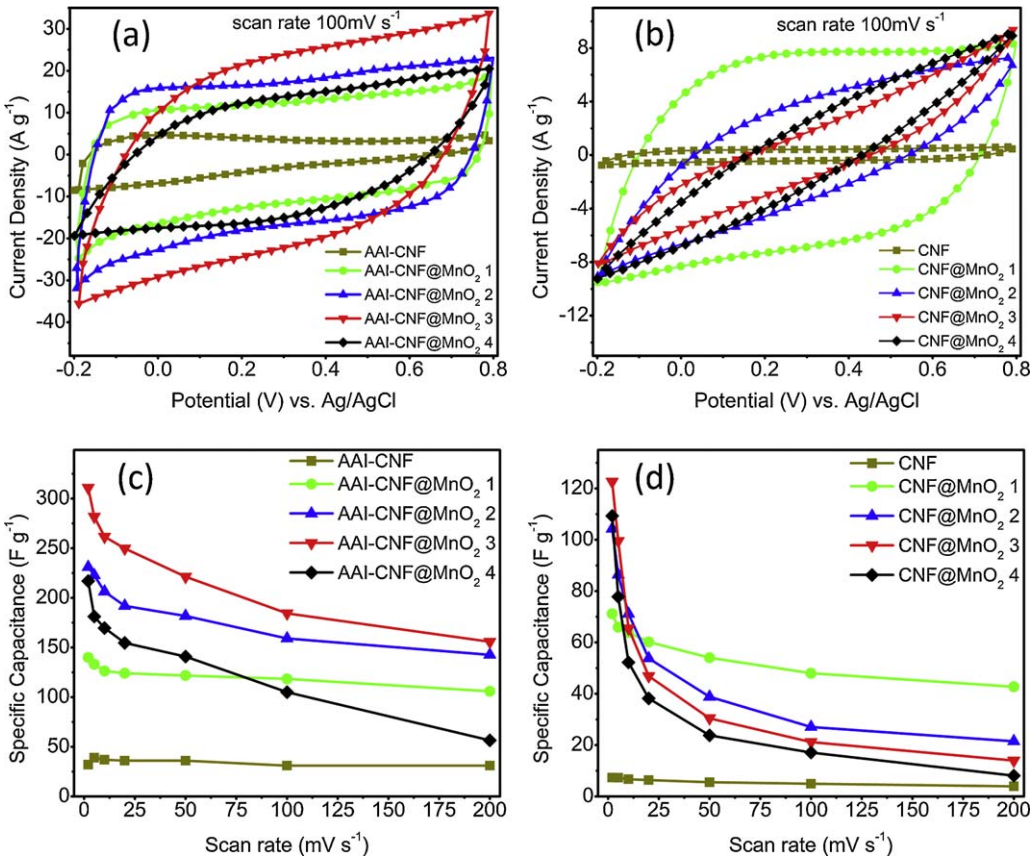


**Fig. 4.** CV curves of the electrodes at a scan rate of 100 mV $s^{-1}$ for AAI-CNF@$MnO_2$ (a) and CNF@$MnO_2$ (b); Specific capacitance of the electrodes as a function of scan rate for AAI-CNF@$MnO_2$ (c) and CNF@$MnO_2$ (d).

mance in specific capacitance and rate capability. Large capacitance loss was observed when increasing the scan rate. For example, at ~23 wt% of $MnO_2$ loading at 200 mV $s^{-1}$, the AAI-CNF@$MnO_2$ electrode 2 showed 142 F $g^{-1}$ of capacitance, corresponding to 61% of rate capability while CNF@$MnO_2$ 2 had only 21 F $g^{-1}$ capacitance, corresponding to 20% of rate capability.

To evaluate the contribution of the active $MnO_2$ to the electrode capacitance, the specific capacitances of the $MnO_2$ shell were extracted following the method reported [25]. Fig. 5 represents the dependence of the specific capacitance of the $MnO_2$ shell on the loading at a scan rate of 2 mV $s^{-1}$. The specific capacitance of the $MnO_2$ shell on the AAI-CNF surface reached 808 F $g^{-1}$ at 13.9% of oxide loading, and increased to 900 F $g^{-1}$ at 23.0% of oxide loading. The values were close to the results reported by Lee et al. [13] using CNT and far better than other results obtained from CNF, graphene and $Zn_2SnO_4$ [16,17,23,26]. Further increase in the $MnO_2$ loading reduced the $MnO_2$ specific capacitance. 746 F $g^{-1}$ and 345 F $g^{-1}$ were observed at 39.1% and 59.0% of oxide loading, respectively. Similar trend was observed previously [21,25]. This was due to the fact that too thick oxide coating caused part of material to be electrochemically inactive, and jeopardized the charge transport.

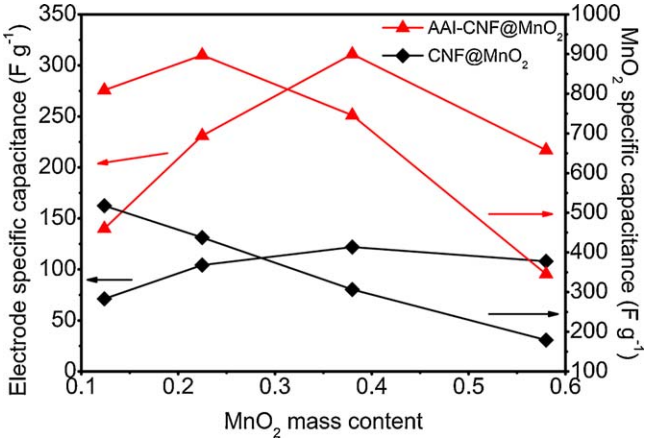


**Fig. 5.** Specific capacitance for the electrodes and the pristine $MnO_2$ of the AAI-CNF@$MnO_2$ and CNF@$MnO_2$ samples, data were derived from CV scan at 2 mV $s^{-1}$.

The electrochemical behavior observed can be interpreted with the redox reactions associated with $MnO_2$. Considering the pseudocapacitance mechanisms of $MnO_2$ in $Na_2SO_4$ aqueous electrolyte, the following reactions may occur [12]

$$MnO_{2\,surface} + Na^+ + e^- = MnO_2{}^-Na^+{}_{surface} \quad \text{(surface absorption)} \tag{2}$$

$$MnO_{2\,bulk} + Na^+ + e^- = MnOONa_{bulk} \quad \text{(bulk ion intercalation)} \tag{3}$$

Simultaneous transfer of $Na^+$ cation and electrons to $MnO_2$ is the key to completing the charge storage reaction. Reaction (2) can be achieved by increasing the $MnO_2$ surface area exposed to the electrolyte, which would be realized by our high specific surface area of AAI-CNF support. Also, a thin and porous $MnO_2$ sheath and the nano-whisker structures shorten the ion diffusion pathway. Reaction (3) requires the fast electron transport inside the carbon backbone to effectively transfer electrons to the $MnO_2$ phase. In our study, $MnO_2$ are in situ formed both on the AAI-CNF or CNF surface, which enhances the intimate contact between carbon and

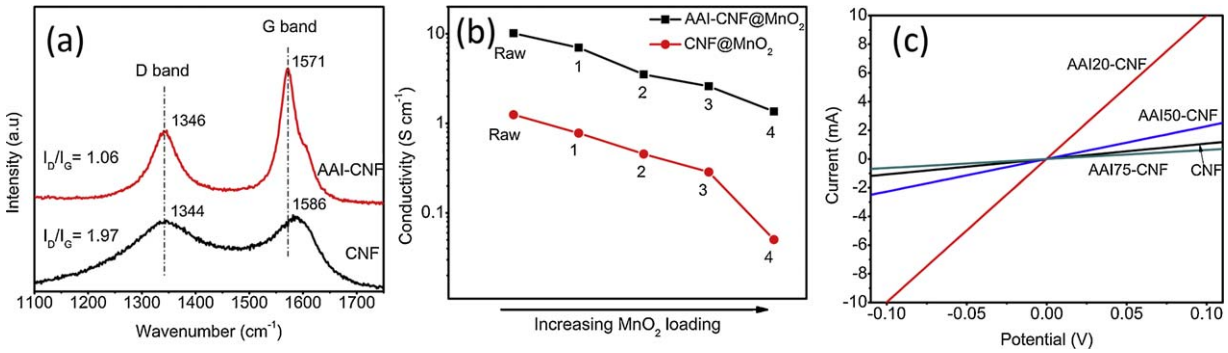


**Fig. 6.** (a) Raman spectra of the AAI-CNF and CNF; (b) conductivity of the AAI-CNF@$MnO_2$ and CNF@$MnO_2$ electrodes, (c) *V–I* curves of the carbon nanofibers with different amount of AAI loading the precursor. The numbers are the mass ratio of the AAI to PAN.

$MnO_2$. However, the electron transfer rates in AAI-CNF and CNF are different. If the electron mobility is low in the carbon backbone, the charge storage process will be inefficient. In order to better understand the mechanism, Raman spectra were taken from AAI-CNF and CNF (Fig. 6(a)). Both the *D* band and *G* band of the AAI-CNF were narrow and sharp while the peaks of CNF were broad, which indicated the ordered and crystalline nature of the carbon structure in AAI-CNF. The *D* band of the AAI-CNF and CNF was at 1346 $cm^{-1}$ and 1344 $cm^{-1}$. The G band of the AAI-CNF red shifted 15 $cm^{-1}$ compared to that of CNF. The $I_D/I_G$ ratio (the peak intensity ratio) was 1.97 for AAI-CNF and 1.06 for CNF, which confirmed that more ordered graphite phase was presented in the AAI-CNF.In addition, the AAI-CNF and CNF electrodes had conductivity of 10.14 S $cm^{-1}$ and 1.25 S $cm^{-1}$ before $MnO_2$ coating, respectively. The conductivity of the electrodes dropped with an increase in the $MnO_2$ loading (Fig. 6(b)). However, due to higher conductivity of the AAI-CNF core, the AAI-CNF@$MnO_2$ composite samples exhibited better conductivity than the CNF@$MnO_2$ counterparts. Therefore, it can be concluded from Fig. 6(a) and (b) that the more ordered graphite content in AAI-CNF is responsible for the enhanced electrode conductivity. Furthermore, the effect of the different AAI content in the electrospinning precursor on the conductivity of the product was examined. Fig. 6 (c) shows the corresponding *V–I* curves of the carbon nanofibers with different amount of AAI loading in the precursor. It was found that the 2 wt% AAI in the precursor (or 20 wt% relative to PAN) which was used in current investigation was the optimized value. Excess AAI will lead to the formation of more insulating $Fe_3O_4$ phase in the nanofibers [27].

Impedance analysis was carried out to further understand the effect of the AAI addition on the performance enhancement. The Nyquist plots of two sets of samples are presented in Fig. 7(a) and (b). The series resistance and the charge transfer resistance of the electrode can be separated using Nyquist plot. The AAI-CNF@$MnO_2$ electrodes had nearly ideal linear shape with the phase angle close to 80° at 0.01 Hz. No evident semicircle corresponding to charge transfer resistance was found. However, the CNF@$MnO_2$ electrodes exhibited a non linear behavior accompanied by visible semicircles at a high frequency regime, showing almost two times larger series resistance. The charge transfer resistances estimated from the diameter of the semicircles were 4, 5, 9 and 14 ohms with increasing the $MnO_2$ loading. From the Nyquist plots, the capacitance retardation in the CNF@$MnO_2$ samples was due to two problems: (i) high series resistance attributed to insufficient conductivity of the electrode, especially at a high $MnO_2$ loading, and (ii) large charge transfer resistance at the carbon/$MnO_2$ interface that inhibits the $Na^+$ insertion/adsorption process in $MnO_2$, leading to capacitance degradation at a high operation rate. The two problems were mitigated by the addition of AAI into CNF. The conductivity of the AAI-CNF (1.35 S $cm^{-1}$) was almost 27 times higher than CNF (0.05 S $cm^{-1}$) even at high $MnO_2$ loading (59% of $MnO_2$ loading), which minimized the series resistance of the electrode, reducing the IR loss. In addition, the AAI-CNF@$MnO_2$ samples showed an almost linear shape in the Nyquist plot in the absence of an evident semicircle, which indicated a negligible charge transfer resistance. Benefited from the higher surface area of the AAI-CNF backbone, the C/$MnO_2$ contact area can be enlarged and the interfacial resistance between carbon and $MnO_2$ can be reduced, therefore the electron and ions can be more easily transferred.

Complex Bode plots were also used to study the rate capability of the electrodes. The impedance of a supercapacitor device can be expressed as [30]

$$Z = \frac{1}{j\omega C}$$

where *C* is the device capacitance, $\omega$ is the radius speed, the equation then yields

$$C = \frac{1}{j\omega Z} = \frac{Z''}{\omega|Z|^2} - \frac{jZ'}{\omega|Z|^2}$$

Herein the total capacitance of the device can be written as

$$C = C' - jC'',$$

where $C' = Z''/\omega|Z|^2$ and $C'' = Z'/\omega|Z|^2$.

The real part $C'$ is defined as the effective capacitance that the device can delivery, and the imaginary part $C''$ is related to the irreversible resistivity loss in the device. The frequency $f$ is the character frequency at which $C''$ reached the maximum, and $\tau = 1/f$ is the time constant of the device, which are characteristic of the rate capability [30]. High power density supercapacitors generally possess high character frequency and smaller $\tau$ [31,32]. Fig. 7(c) is the $C'$ curves of the AAI-CNF@$MnO_2$ electrodes. The capacitances derived from the $C'$ curves are similar to the results obtained from CV curves. The AAI-CNF@$MnO_2$ electrode (Sample 3) exhibited the highest capacitance of ~252 mF at 0.01 Hz. The CNF@$MnO_2$ sample in Fig. 7(d) showed much less capacitance, which indicated that the electrode's usable capacitance was low even at a frequency of 0.01 Hz. This was consistent with the CV measurements. The character frequencies of the AAI-CNF@$MnO_2$ electrodes were calculated from Fig. 7(e). The AAI-CNF had a character frequency of 0.48 Hz and a time constant of 2.08 s, which was better than 0.1 Hz and 10 s for the activated carbon electrode reported previously [30]. After coating with $MnO_2$, the $C''$ curves peak shifted to lower frequency because of the increased capacitance. However, the $f$ of the AAI-CNF@$MnO_2$ could be kept at reasonable range. For example, the character frequency of the four electrodes are 0.40, 0.20, 0.10 and 0.06 Hz, corresponding to the time constant of 2.5, 5, 10 and 16.7 s, which was comparable to the activated carbon where

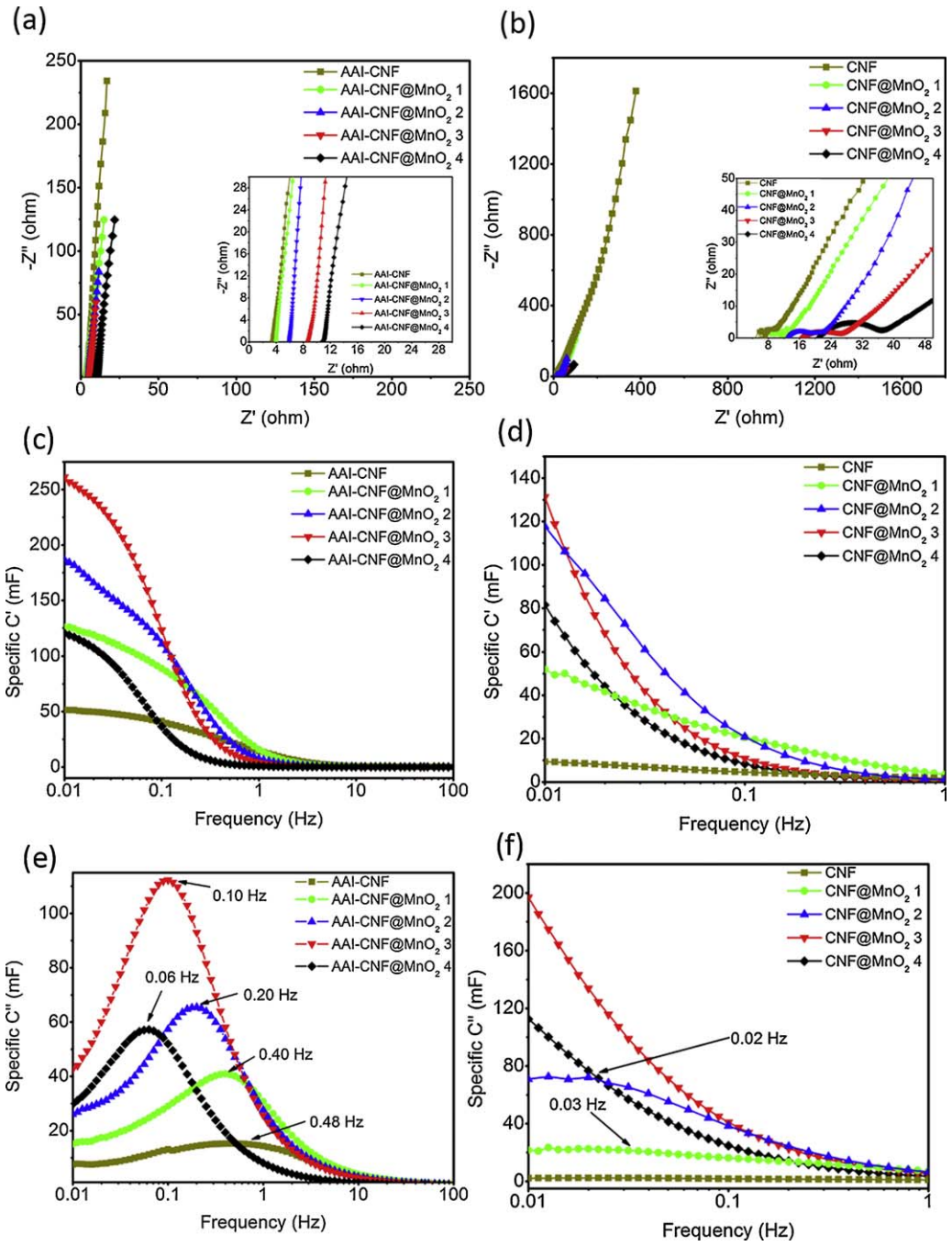


**Fig. 7.** (a) Impedance Nyquist plots of the AAI-CNF@$MnO_2$ electrodes, (b) impedance Nyquist plots of the CNF@$MnO_2$ electrodes, (c) real part in Bode plots of the AAI-CNF@$MnO_2$ electrodes, (d) real part in impedance Bode plots of the CNF@$MnO_2$ electrodes, (e) imaginary part in impedance Bode plots of the AAI-CNF@$MnO_2$ electrodes, and (f) imaginary part in impedance Bode plots of the CNF@$MnO_2$ electrodes.

no charge transfer process occurred (10 s), and was similar to the $FeO_x$/carbon nanofoam electrodes (10–22 s) [33]. In the mean time, the CNF@$MnO_2$ electrode showed much slower response in Fig. 7(f). For example, the CNF@$MnO_2$ electrodes (Samples 1 and 2) only showed broad peaks with the character frequency of 0.02 Hz and 0.03 Hz when the other two were far below the lowest testing frequency of 0.01 Hz. This implied that the AAI-CNF $MnO_2$ electrodes (Samples 1 and 2) were able to delivery energy almost 10 times faster than their CNF@$MnO_2$ counterparts [30], despite of the identical sample preparation process and $MnO_2$ loading.

Stability testing was performed on the AAI-CNF@$MnO_2$ electrodes under the constant charge and discharge at 10 A $g^{-1}$ of current density with relative to the total electrode mass (Fig. 8(a)). Except for the AAI-CNF@$MnO_2$ Sample 1, all other electrodes showed over 96% retention after 1000 cycles. The AAI-CNF@$MnO_2$ (Sample 3) electrodes showed the highest capacitance of 209 F $g^{-1}$ and remained 97.6% of its original value after cycling, which was comparable to high-performance $Co_3O_4$@$MnO_2$ [13] and CNT/$MnO_2$ electrode [22]. Fig. 8(b) shows the Ragone plots were of the AAI-CNF@$MnO_2$ Samples 1 and 3. The AAI-CNF@$MnO_2$ electrode (Sample 3) had an energy density of 43.2 Wh $kg^{-1}$ at a power density of 0.31 kW $kg^{-1}$. The power density can be eventually improved to 15.6 kW $kg^{-1}$ at an energy density of 21.7 Wh $kg^{-1}$. The AAI-CNF@$MnO_2$ electrode (Sample 1) showed an energy density of 19.5 Wh $kg^{-1}$ at 0.15 kW $kg^{-1}$, and 14.6 Wh $kg^{-1}$ at 10.6 kW $kg^{-1}$. However, when considering the active $MnO_2$ shell alone, the energy

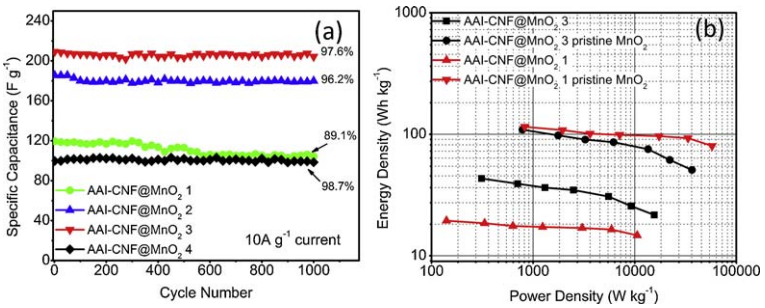


**Fig. 8.** (a) Stability of the AAI-CNF@$MnO_2$ electrodes; (b) Ragone plots of the AAI-CNF@$MnO_2$ electrodes.

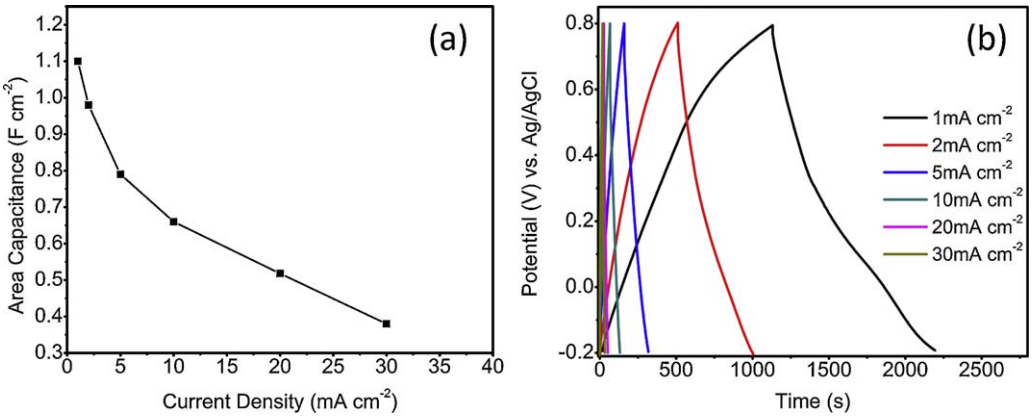


**Fig. 9.** (a) Area-capacitance of the AAI-CNF@$MnO_2$ electrode (Sample 3) at different current densities, (b) is the charge–discharge curves.

and the power density reached 115.6 Wh $kg^{-1}$ at 0.83 kW $kg^{-1}$ and 80.2 Wh $kg^{-1}$ at 57.7 kW $kg^{-1}$. This was superior to most recently reported values based on pristine $MnO_2$ supported on CNT [34], graphene [16,17] and $Zn_2SnO_4$ [23].

Finally we constructed an electrode with 2.5 mg of AAI-CNF@$MnO_2$ (Sample 3) and tested the area-capacitance at different current densities (Fig. 9). The electrode had 1.1 F $cm^{-2}$ of area-capacitance at 1 mA $cm^{-2}$ of current density, which was comparable to the highest value (0.8–7 F $cm^{-2}$) for $MnO_2$-based electrode [15,22,35]. The electrode showed 0.38 F $cm^{-2}$ of area-capacitance at 30 mA $cm^{-2}$ current density. The coulomb efficiency was kept nearly 1 at all current densities. In the previous reports, the high performance of the electrode was achieved only at a small area or volumetric scale [13,23]. In contrast, the AAI-CNF@$MnO_2$ electrode has a great potential of scale-up and can find practical application.

## 4. Conclusions

This work demonstrated a simple, inexpensive and scale-up method that is able to be performed at an ambient condition for fabrication of a $MnO_2$ based electrode for a high power and energy density pseudo-supercapacitor. The electrochemical tests showed that the addition of the iron compound into the CNF greatly improved the electronic conductivity of the CNF, and facilitated the charge transfer between the metal oxide and the CNF, reducing the internal resistance of the electrode at a high $MnO_2$ loading. In addition, the addition of the iron compound also increased the specific surface area of the CNF. Enhancement of the conductivity of the CNF dramatically improved the rate capability and the power density of the CNF/$MnO_2$ coaxial cable electrode. The AAI-CNF@$MnO_2$ electrode with 13.9 wt% of $MnO_2$ loading exhibited 76% of specific capacitance when the scan rate increased from 2 mV $s^{-1}$ to 200 mV $s^{-1}$. This rate capability was better than the previously reported CNF/metal oxide coaxial electrodes that suffered from huge performance degradation with increasing the operation rate. The AAI-CNF/$MnO_2$ electrode also showed an enhanced specific capacitance of 311 F $g^{-1}$ for the whole electrode and 900 F $g^{-1}$ for the $MnO_2$ shell at a scan rate of 2 mV $s^{-1}$. We believe the results demonstrated here have implications in design of CNF/metal oxide-based electrodes for energy storage devices.

## Acknowledgements

The resource and facilities used were partially supported by a Research Challenge Grant from the State of West Virginia (EPS08-01) and the West Virginia University Research Corporation and the West Virginia EPSCoR Office.

## References

[1] M. Jayalakshmi, K. Balasubramanian, Int. J. Electrochem. Sci. 3 (2008) 1196–1217.
[2] G.P. Wang, L. Zhang, J.J. Zhang, Chem. Soc. Rev. 19 (2012) 797–828.
[3] S. Patrice, G. Yury, Nat. Mater. 7 (2008) 845–854.
[4] E. Frackowiak, F. Beguin, Carbon 39 (2001) 937–950.
[5] J.H. Kim, S.H. Kang, K. Zhu, J.Y. Kim, N.R. Neale, A.J. Frank, Chem. Commun. 47 (2011) 5214–5216.
[6] Y.G. Wang, X.G. Zhang, Electrochim. Acta 49 (2004) 1957–1962.
[7] V. Subramanian, H.W. Zhu, B.Q. Wei, J. Power Sources 159 (2006) 361–364.
[8] J.T. Li, W. Zhao, F.Q. Huang, A. Manivannan, N.Q. Wu, Nanoscale 3 (2011) 5103–5109.
[9] H. Jiang, T. Zhao, J. Ma, C.Y. Yan, C.Z. Li, Chem. Commun. 47 (2011) 1264–1267.
[10] M.S. Wu, Z.S. Guo, J.J. Jow, J. Phys. Chem. C. 114 (2010) 21861–21867.
[11] W.F. Wei, X.W. Cui, W.X. Chen, D.G. Ivey, Chem. Soc. Rev. 40 (2011) 1697–1721.
[12] M. Toupin, T. Brousse, D. Bélanger, Chem. Mater. 16 (2004) 3184–3190.
[13] S.W. Lee, J.Y. Kim, S. Chen, P.T. Hammond, Y. Shao-Horn, ACS Nano 4 (2010) 3889–3896.
[14] W. Chen, Z.L. Fan, L. Gu, X.H. Bao, C.L. Wang, Chem. Commun. 46 (2010) 3905–3907.
[15] X.B. Jin, W.G. Zhou, S.W. Zhang, G.Z. Chen, Small 3 (2007) 1513–1517.
[16] G.H. Yu, L.B. Hu, M. Vosgueritchian, H.L. Wang, X. Xie, J.R. McDonough, X. Cui, Y. Cui, Z.N. Bao, Nano Lett. 11 (2011) 2905–2911.

[17] G.H. Yu, L.B. Hu, N. Liu, H.L. Wang, M. Vosgueritchian, Y. Yang, Y. Cui, Z.N. Bao, Nano Lett. 11 (2011) 4438–4442.
[18] Q. Li, J.H. Liu, J.H. Zou, A. Chunder, Y.Q. Chen, L. Zhai, J. Power Sources 196 (2011) 565–572.
[19] A.E. Fischer, K.A. Pettigrew, D.R. Rolison, R.M. Stroud, J.W. Long, Nano Lett. 7 (2007) 281–286.
[20] R.B. Rakhi, D.K. Cha, W. Chen, H.N. Alshareef, J. Phys. Chem. C 115 (2011) 14392–14399.
[21] X.Y. Lang, A. Hirata, T. Fujita, M.W. Chen, Nat. Nanotechnol. 6 (2011) 232–236.
[22] J.P. Liu, J. Jiang, C.W. Cheng, H.X. Li, J.X. Zhang, H. Gong, H.J. Fan, Adv. Mater. 23 (2011) 2076–2081.
[23] L.H. Bao, J.F. Zang, X.D. Li, Nano Lett. 11 (2011) 1215–1220.
[24] J. Yan, E. Khoo, A. Sumboja, P.S. Lee, ACS Nano 4 (2010) 4247–4255.
[25] A. Ghosh, E.J. Ra, M.H. Jin, H.K. Jeong, T.H. Kim, C. Biswas, Y.H. Lee, Adv. Funct. Mater. 21 (2011) 2541–2547.
[26] J.G. Wang, Y. Yang, Z.H. Huang, F.Y. Kang, Electrochim. Acta 256 (2011) 9240–9247.
[27] J.E. Panels, J. Lee, K.Y. Park, S.Y. Kang, M. Marquez, U. Wiesner, Y.L. Joo, Nanotechnology 19 (2008) 455612.
[28] J. Yan, Z.J. Fan, W. Tong, W.Z. Qian, M.L. Zhang, F. Wei, Carbon 48 (2010) 3825–3833.
[29] N.Q. Wu, L. Fu, M. Su, M. Aslam, K.C. Wong, V.P. Dravid, Nano Lett. 4 (2004) 383–386.
[30] C. Portet, P.L. Taberna, P. Simon, E. Flahaut, C. Laberty-Robert, Electrochim. Acta 50 (2005) 4174–4181.
[31] J.R. Miller, R.A. Outlaw, B.C. Holloway, Science 329 (2010) 1637–1639.
[32] Y. Honda, T. Haramoto, M. Takeshige, H. Shiozaki, T. Kitamura, M. Ishikawa, Electrochem. Solid-State Lett. 10 (2007) A106–A110.
[33] M.B. Sassin, A.N. Mansour, K.A. Pettigrew, D.R. Rolison, J.W. Long, ACS Nano 4 (2010) 4505–4514.
[34] H.N. Alshareef, W. Chen, R.B. Rakhi, L.B. Hu, X. Xie, Y. Cui, Nano Lett. 11 (2011) 5165–5172.
[35] L.B. Hu, W. Chen, X. Xie, N. Liu, Y. Yang, H. Wu, Y. Yao, M. Pasta, H.N. Alshareef, Y. Cui, ACS Nano 5 (2011) 8904–8913.